Author's Accepted Manuscript

A facile in situ synthesis of nanocrystal-FeSi-embedded Si/SiO$_X$ anode for long-cycle-life lithium ion batteries

Wei He, Yujia Liang, Huajun Tian, Shunlong Zhang, Zhen Meng, Wei-Qiang Han

Cite this article as: Wei He, Yujia Liang, Huajun Tian, Shunlong Zhang, Zhen Meng and Wei-Qiang Han, A facile in situ synthesis of nanocrystal-FeSi-embedded Si/SiO$_X$ anode for long-cycle-life lithium ion batteries, *Energy Storage Materials,* http://dx.doi.org/10.1016/j.ensm.2017.05.003

A facile in situ synthesis of nanocrystal-FeSi-embedded Si/SiO$_x$ anode for long-cycle-life lithium ion batteries

Wei He,[a] Yujia Liang,[b] Huajun Tian,[a,*] Shunlong Zhang,[a,c] Zhen Meng,[a] and Wei-Qiang Han,[a, c, d, *]

[a]*Ningbo Institute of Materials Technology and Engineering, Chinese Academy of Sciences, Ningbo 315201, P. R. China*

[b]*Department of Chemical and Biomolecular Engineering, University of Maryland, College Park, Maryland 20742, United States*

[c]*School of Physical Science and Technology, Shanghai Tech University, Shanghai 200031, P. R.China*

[d]*School of Materials Science and Engineering, Zhejiang University, Hangzhou 310027, P. R. China*

tianhuajun@nimte.ac.cn;

hanwq@zju.edu.cn

*Corresponding Authors.

Abstract

A cost-effective, environmentally friendly and industrialized method of using low-grade sources to prepare high-performance anode material for lithium ion batteries (LIBs) with high energy density and long cycle life is both appealing and challenging. Herein, we present a low-cost, scalable and controllable approach for preparing unique sub-micrometer core-shell structure nanocrystal-FeSi-embedded Si/SiO$_x$ (FSO) anode material directly from a low-grade Fe-Si alloy. The sub-micrometer FSO anode materials are controlled by in-situ reaction of the Fe-Si-O in the Fe-Si alloy according to the phase diagram. The XRD and Rietveld refinement results indicate that when the treatment temperature increase, (i) FeSi phase appears together with Si and FeSi$_2$, and then (ii) Fe$_3$Si phase appears together with Si and FeSi. Most importantly, benefited from the formation of the amorphous SiO$_x$ as buffer layer and self-conductive nanocrystal-FeSi as a robust skeleton to

mechanically support the large volume change of Si during cycling, the sub-micrometer core-shell structure FSO anode exhibits a high capacity (931.3 mAh g^{-1}) at 50 mA g^{-1} and a prolonged cycle performance with 86% capacity retention over 1000 cycles at 1 A g^{-1}. The full cell with prelithiated FSO as the anode and commercial $LiCoO_2$ as the cathode delivers a high energy density of 467.5 Wh kg^{-1} at the 0.05 C. This work provides a promising route for commercial production of high-performance Si/SiO_x-based anode materials in LIBs.

Keywords:

lithium ion batteries; anodes; Si/SiO_x; Fe-Si alloy; core-shell structure

Introduction

To meet the ever-growing demands for electric vehicles (EVs), portable electronics, and large-scale renewable energy storage, it is urgent to develop the next generation lithium ion batteries (LIBs) with low cost, high energy density, and long cycle life.[1-5] Among anode materials, silicon has attracted the most attention due to its high theoretical capacity (3579 mAh g^{-1}), with the potential to significantly improve the performance of LIBs.[6, 7] However, the bulk silicon anodes experience over 300% volume change during the lithiation and delithiation processes, which leads to particle pulverization, loss of interparticle electrical contact, and instability of the solid electrolyte interphase (SEI), resulting in repeating chemical side reactions with the electrolyte and fast capacity fading.[8-10] To address these issues, a wide range of strategies have been developed to improve the electrochemical performances of Si-based anodes, including: (1) decreasing the size of Si-based materials to the nano-scale;[11, 12] (2) coating protective materials as a buffer layer to mitigate the considerably large volume expansion;[13-16] (3) designing porous structure, hollow structure, core-shell structure Si materials.[17, 18] Nanocrystallization and protective materials coating has been widely researched to show that they are able to address the issues of Si-based anodes. Nano-sized silicon materials demonstrate higher cycling stability, since they can prevent fractures during the large volume changes.[19] They differ from corresponding bulk Si materials, and behave abnormally due to surface and interface effect as well as size effectiveness that the volume expansion of silicon anodes can be alleviated when the size of silicon is below 150 nm.[20] However, the usage

of nano-sized silicon in anodes for LIBs is still hard to commercialize due to their complex synthesis processes with low production rates, high cost, and low gravimetric and volumetric energy densities.[21] Recently, some strategies using micrometer/sub-micrometer Si-based materials in LIBs have exhibited some progress.[22-25] Furthermore, SiO_x as a buffer to enhance the electrochemical performance of Si-based materials has attracted a lot of attention.[26-29] The existence of the amorphous the SiO_x structure is favorable for providing good cycling stability, because the less active amorphous SiO_x can effectively accommodate the large volume expansion of the Si during cycling.[27, 30-32] Simultaneously, a highly stable SEI can be formed on the surface of the amorphous SiO_x, avoiding repeated formation of SEI film during cycles, which would lead to a decline in capacity.[33-35] For instance, Kim *et al.* prepared a core-shell structure Si/SiO_x nanocomposite via sol-gel reaction of triethoxysilane with commercially available Si nanoparticles, providing a high capacity (1914 mAh g^{-1}) with a notably improved initial coulombic efficiency (from 47.6% to 73.6%), and stable cycle performance over 100 cycles without carbon coating.[36] Shin et al. provided a catalyst-free synthesis of core-shell Si-SiO_x nanowires, which was directly grown on the thick copper foils by the evaporation of SiO powder using thermal chemical vapor deposition (CVD). The core-shell Si-SiO_x nanowire exhibited a stable cycle performance with 95% capacity retention over 100 cycles[37]. Similarly, Park *et al.* reported a highly interconnected Si/SiO_x nanowire by combining thermal disproportionation of SiO with metal-catalyzed Si nanowire growth. The Si/SiO_x electrodes showed a reversible capacity of 1280 mAh g^{-1} after 150 cycles at a rate of 0.2 C, and a high rate capability of ~1200 mAh g^{-1} at 10 C rate.[38] However, there are still some problems of the Si/SiO_x nanocomposite, such as the poor conductivity, complicated synthesis process and high preparation cost, which limit their practical applications.

Herein, instead of preparing nanoparticles, we report a new approach for creating high-capacity sub-micrometer core-shell structure nanocrystal-FeSi-embedded Si/SiO_x (FSO) anode materials according to phase diagram, using the abundant and inexpensive metallurgical Fe-Si alloy as Si/SiO_x source. The SiO_x shell for the buffer layer is obtained by the oxidation of the silicon on the surface of Fe-Si alloy during heating in ambient air, with the formation of nanocrystal-FeSi by in-situ reaction of the $FeSi_2$ with controlled phase transformation of Fe-Si alloy. Most importantly, the core-shell structure and self-conductive nanocrystal-FeSi usage as a robust mechanical skeleton can effectively avoid particle fracture, providing excellent cycling stability with 99.4% capacity retention over 500

cycles at 500 mA g^{-1} and 86% capacity retention over 1000 cycles at 1 A g^{-1}, which is one of the best performances among the micrometer/sub-micrometer Si/SiO$_x$ anode materials reported. Note that our preparation method of amorphous SiO$_x$ shell is novel, cost-effective, scalable, and it is possible to implement for future scale-up manufacturing. This process provides the possibility to commercialize the long-lasting Si/SiO$_x$ anodes for LIBs with high gravimetric and volumetric energy densities.

Experimental section

Fabrication of FSO Anode Materials

The FSO anode materials were prepared by mechanical milling and heat treatment of commercial Fe-Si alloy sources (~1000 $/t) under ambient conditions, as illustrated in **Figure S1.** The Fe-Si alloy powders (73.3% Si, 21.4% Fe and other impurities) were obtained from a metallurgical factory. Firstly, the bulk Fe-Si alloy powders were crushed by ball milling (PM200, Retsch GmbH Inc., Germany) in order to obtain sub-micrometer Fe-Si alloy particles. After that, the sub-micrometer Fe-Si alloy particles were calcined under ambient conditions at 800 ^{o}C for 3 h, resulting in the oxidation of silicon on the surface of Fe-Si alloy. Thus, the final product of sub-micrometer core-shell structure FSO was obtained. In order to investigate the mechanism of the formation of core-shell FSO controlled by iron-silicon-oxygen phase transition, we prepared FSO under different temperatures including 400 ^{o}C, 600 ^{o}C, 1000 ^{o}C, and marked them as FSO-400, FSO-600 and FSO-1000. FSO only represent that the Fe-Si alloy which is calcined at 800 ^{o}C in this paper.

Electrochemical Measurements of the as-prepared FSO Anode Materials

To make a working electrode, an aqueous slurry method was used. FSO, carboxyl methyl cellulose (CMC), and carbon black with a mass ratio of 80: 10: 10 were stirred for over 12 h to ensure thorough mixing. The slurry was casted onto a thin copper foil and dried. Prior to cell fabrication, the electrodes were dried in a vacuum oven at 110 °C overnight. The coin cells were assembled with lithium foil as the counter electrode, 1.0 M LiPF$_6$ solution in a mixture of fluoroethylene carbonate/dimethyl carbonate/ethyl methyl carbonate (FEC/DMC/EMC, 1:1:1 in volume) or ethylene carbonate/diethyl carbonate (EC/DEC, 1:1 in volume) with 5 % FEC electrolyte as the electrolyte, and a polypropylene film (Celgard-2300) was used as a separator. The coin cells were assembled in an argon-filled glove box. The electrochemical properties of the FSO materials were studied with a

multichannel battery-testing system (LAND CT2000, Wuhan LAND electronics Co., China). FSO materials were evaluated using charge/discharge galvanostatic cycling from 1.5 V to 0.01 V with loading masses of ~ 1.0 mg cm^{-2}, 1.51 mg cm^{-2} and 1.98 mg cm^{-2}. EIS was taken using a Solartron 1470E Electrochemical Interface (Solatron Analytical, UK) electrochemical workstation at 25 °C with the frequency ranging from 1 MHz to 0.001 Hz and an AC signal of 10 mV in amplitude as the perturbation. Cyclic voltammogram was carried out using Solartron 1470E Electrochemical Interface (Solartron Analytical, UK), the voltage was canned at 0.1 mV s^{-1} between 0.01~1.5 V for 5 cycles.

Electrochemical Measurements of the full cell

The commercial LiCoO$_2$ electrodes were prepared using the similar slurry method. 80% commercial LiCoO$_2$, 10% carbon black and 10% polyvinylidene fluoride (PVDF) were stirred for over 12 h to ensure thorough mixing. The slurry was casted onto a thin aluminium foil and dried in vacuum oven at 110 °C overnight. Before being used in the full cell, the FSO electrodes were undergone pre-lithiation in order to suppress the first irreversible capacity loss. The full cell were assembled into a type CR2032 coin cell with the prepared FSO as the anode and the LiCoO$_2$ as the cathode, 1.0 M LiPF$_6$ solution in a mixture of fluoroethylene carbonate/dimethyl carbonate/ethyl methyl carbonate (FEC/DMC/EMC, 1:1:1 in volume) as the electrolyte, and a polypropylene film (Celgard-2300) was used as a separator. Note that the N/P (negative electrode capacity/positive electrode capacity) radio was ~ 1.2. The full cells were evaluated using charge/discharge galvanostatic cycling between 2.5 and 4.2 V.

Structure Characterization

XRD measurements were performed with a Bruker D8 Advance powder diffractometer using Cu$K\alpha$ sealed tube radiation (λ = 1.5418 Å) and Ni β-filter and equipped with LynxEye position sensitive detector. Rietveld refinement was conducted to determine the composition of the powders using Topas-5 software from Bruker. Thermogravimetric analysis (TGA) was carried out using a Perkin Elmer Diamond TG/DTA instrument at a heating rate of 10 ^{o}C min^{-1} under ambient conditions. X-ray photoelectron spectroscopy (XPS) measurements were carried out on an Axis Ultra DLD imaging photoelectron spectrometer. The samples were characterized by using scanning electron microscopy (FESEM and HR-SEM, Hitachi, S-4800) and transmission electron microscopy (TEM, FEI Ltd., Tecnai F20).

Results and discussion

We demonstrated a new approach for creating a sub-micrometer core-shell structure FSO anode guided by phase diagram by using abundant and inexpensive metallurgical Fe-Si alloy, shown in **Figure 1**. This process can produce over 500 g of FSO anode material per batch (**Figure 2a**). The XRD curve of the pristine Fe-Si alloy powder is shown in **Figure 2b** (black curve). The three relatively high intensity diffraction intensity peaks (28.4^o, 47.3^o, and 56.1^o) are attributed to the crystalline Si (crystal phase PDF#27-1402). Four weaker diffraction peaks at 17°, 38°, 48° and 49° correspond to the (001), (101), (110) and (102) of the $FeSi_2$ (PDF#35-0822) in the Fe-Si alloy. Since Si accounts for 73.3 wt% (87.3 wt%) in the Fe-Si alloy, the equilibrium phases expected at room temperature are $FeSi_2$ and Si based on phase diagram (zone (1) in **Figure S2**), which is consistent with the XRD results. When the calcination temperature was 400 ^{o}C, SiO_x is formed with an amorphous background at around 23° on the XRD curve (red curve, **Figure 2b**). Similar results have also been reportedregarding amorphous SiO_x in XRD results.[40] For the observation of only Si oxides, both the higher atomic percent of Si in the alloy and the higher reactivity of Si towards oxygen (based on Ellingham diagram[41]) could be the causes. Si and $FeSi_2$ remain the main phases at 400 ^{o}C. When the temperature increases to 600 ^{o}C, FeSi phase appears together with Si and $FeSi_2$ (green curve, **Figure 2b**). According to the phase diagram (**Figure S2**), the appearance of FeSi phase indicates a decrease of Si wt% in the alloy, compared with the pristine Fe-Si powders. Once the Si wt% decrease to the range from 50 % to 66.7 %, which is less than Si wt% before calcination (87.3 wt%), the equilibrium phases will become FeSi and $FeSi_2$.[39] To validate this hypothesis, Rietveld refinement is conducted based on the XRD curve obtained at 600 ^{o}C. The results are shown in **Figure 2c** and **Table S1**. From Table S1, Si element accounts for 84 wt% in the alloy at 600 ^{o}C, which means zone (1) in the phase diagram is more representative of the condition of alloy obtained at 600 ^{o}C than zone (2), where FeSi is one of the equilibrium phases. This is attributed to the non-uniformly distributed Fe and Si within the particle. Therefore, the Si wt% is lower in certain locations than that of other areas within the particle. In the locations with lower Si concentrations, the equilibrium phases would be FeSi and $FeSi_2$. Interestingly, chemical changes also occur at these experimental conditions, converting $FeSi_2$ phase into FeSi phase. The chemical reaction process

could be illustrated as:

$$FeSi_2 \xrightarrow{800\ ^oC} FeSi + Si ....(1)$$

With the further increase of treatment temperature to 800 ^oC, the signals from SiO_x become significant, as shown in **Figure 2b** (blue curve). The observation of Fe_3Si means a further decrease of Si atomic percent in the alloy. The equilibrium phases are Fe_3Si and $FeSi$ when the Si wt% is between 25 % and 50 %, located in zone (3) in **Figure S2**.[39] Our Rietveld refinement results show that the Si elemental wt% among the crystal phases of powders is 74 wt % (**Figure 2d** and **Table S3**), which is higher than the theoretical Si atomic percent boundary between the zone (2) and (3). Therefore, the crystal phases observed from XRD can represent all the possible equilibrium phases from zone (1) to (3) in the phase diagram of **Figure S2**. The hump of the amorphous background in **Figure 2b** (blue curve) became more significant, indicating that more SiO_x layers are formed, compared to the XRD patterns of the Fe-Si alloy and FSO. When the temperature is increased to 1000 ^oC, the Fe will be fully oxidized into Fe_2O_3 and Fe_3O_4, for the relative low amount of Fe in the raw materials. Therefore, Fe_2O_3, Fe_3O_4 and SiO_x, SiO_2 and Si are found in the XRD pattern (**Figure 2b**).

To figure out the distribution of Fe and Si over the powders, TEM observations were conducted. The typical morphology of the Fe-Si alloy before calcination is shown in **Figure 2e and Figure S3**. It can be seen that a structure with Fe-Si encapsulated by Si is observed. The bright and dark areas represent the Si and $FeSi_2$, respectively in **Figure 2e**, supported by **Figure S3** with $FeSi_2$ and Si fringes on the corresponding dark and bright areas in **Figure S3a**, respectively. The morphologies of Fe-Si particles after calcination under various temperatures are shown in **Figure 2f-i**, which illustrates the evolution of the powder structure and chemical composition in FSO particles. After the FSO particles were calcined in the muffle furnace at 400 ^oC, the Si in the surface of Fe-Si alloy was partially oxidized into SiO_x layer (marked by black arrow in **Figure 2f**), which has been validated by the amorphous SiO_x background in XRD curve (**Figure 2b**, red curve). The nanocrystal-FeSi was fabricated by in-situ reaction of the $FeSi_2$ in the Fe-Si alloy. Since the Si on the particle surface is oxidized during the heating process (the amorphous layer in **Figure 2f**), the decrease of Si wt% in the alloy is expected, which further verifies the hypothesis made in the XRD results discussion. With the temperature rising to 600 °C, the oxidation rate of Si has been greatly accelerated. The size of Si

oxides increased, as shown in the edge of the sample powder (marked by black arrow) in **Figure 2g**. When the temperature increases to 800 ^oC, a very unique core-shell structure is formed with a Fe-Si core and SiO_x shell (**Figure 2h**). **Figure 3a~e** shows that the sub-micrometer FSO particles consist of a combination of a Fe-Si core, the dispersive nanocrystal-FeSi and a SiO_x shell. The EDS elemental mapping shown in **Figure 3e** also confirms the formation of core-shell structure at 800 ^oC. Moreover, scanning transmission electron microscopy (STEM, **Figure 3f**) supports the core-shell structure with additional evidence provided by O intensity line scans. The statistical analysis of size distribution is provided in the **Figure S4** and the size of the FSO particles ranges from 0.2 μm to 2 μm with an average diameter of 0.48 μm. In a typical FSO particle of ~ 400 nm, the thickness of the SiO_x shell was measured to be at the range of 50 ~ 80 nm and the diameter of the Fe-Si shell was measured to be at the range of 100 ~ 180 nm. When the calcination temperature further increased to 1000 ^oC, the higher oxidation extent of the Fe-Si alloy makes it hard to differentiate the species in TEM (**Figure 2i**). Large aggregates are formed, instead of the structures observed at other temperatures. Our TEM results further confirm the substance evolution during the calcination and the Si wt% decreased with the oxidation of Si on the particle surface. Therefore, phases represented by Zone (3) in the phase diagram were observed instead of those represented by Zone (1) (**Figure S2**). Thermal gravimetric analysis (TGA) data of Fe-Si alloy was carried out under ambient conditions. The TGA curve **(Figure S5**) shows a distinct weight increase at the temperature of 400 °C which corresponds to the oxidation of superficial Si. A transformation mechanism is proposed for the Fe-Si alloy evolution in this work presented in **Figure 1** based on the results above. During the calcination, the Si on the surface of Fe-Si alloy gradually oxidizes to form the SiO_x shell structure. In order to further investigate the valence state of Si in the FSO material, XPS spectrum **(Figure 3g)** is measured. The high resolution XPS spectrum of Si 2p shows two main peaks at 103.1 eV (Si^{4+}) and 102.6 eV (Si^{3+}), which are common features of nonstoichiometric silicon suboxides. A very small peak appeares between 99.0 eV and 100 eV, relating to Si-Si bonding.[42-44] The XPS results indicate that the Fe-Si core definitely were shielded by the SiO_x shell, which is regarded as a nonstoichiometric silicon suboxide amprphous matrix. Overall, it can be seen that the core-shell structure FSO particles could be modified during the phase transformation, which may be one of the best method to prepare unique Si/SiO_x anode for high-performance LIBs.

The electrochemical properties of the core-shell structure FSO anodes for LIBs were evaluated

by cyclic voltammetry (CV) as shown in **Figure 4a**. In the first cathodic scan, there are two small and board peaks at 1.3 V and 0.75 V, which could be attributed to the formation of a thin solid electrolyte interphase (SEI) layer at the electrode/electrolyte interface.[45] During the subsequent cathodic process, a sharp redox peak below 0.1 V corresponds to the formation of the Li_xSi phase. By comparison, an anodic peak at 0.47 V appears, suggesting the reversible delithiation reaction of amorphous Li_xSi phase to the amorphous Si.[46-48] Both cathodic and anodic curves almost overlap completely in the CV scans, indicating the high reversibility and good cycling stability of the core-shell structure FSO anodes.[49] **Figure 4b** shows the charge/discharge voltage profiles of the series FSO composite and pristine Fe-Si alloy at current of 50 mA g^{-1} during the first cycle. The initial Coulombic efficiencies of series FSO composite anodes could be notably improved (66.6%) by controlling the oxidation process. The first discharge potential of FSO rapidly drops to 0.1 V and enters into a long and flat voltage plateau, which is lower than the Fe-Si alloy, corresponding to the formation of the amorphous Li_xSi phase. And the first charge potential of FSO at about 0.4 V corresponds to the formation of the amorphous Si from Li_xSi phase. The first discharge capacity of FSO is 1550 mAh g^{-1} and the first charge capacity is 803 mAh g^{-1}. The irreversible capacity loss is due to the formation of the solid electrolyte interphase (SEI) and chemical reaction of the SiO_x with Li^+ to form lithium-silicate (Li-Si-O). **Figure S6** shows the charge/discharge profiles of the FSO anodes under 800 ^{o}C for different durations including 1 h, 2 h, and 3 h at the first cycle. The initial Coulombic efficiency of FSO anode at 800 ^{o}C for 1 h is 70.3%, indicating that the initial coulombic efficiency can be controlled not only by reaction temperature but also by reaction time, suggesting a way to further improve Coulombic efficiency of the FSO anodes. **Figure 4c** shows the 1st, 10th, 50th and 100th charge/discharge curves of the FSO. The 10th, 50th and 100th charge/discharge curves are almost identical, which means that the FSO anodes have stable and reversible electrochemical behavior, with the agreement of CV curves. **Figure 4d** shows the electrochemical cycling performance of the Fe-Si alloy and the as-prepared FSO anode under different temperatures at a current density of 50 mA g^{-1} for the first 2 cycles and then cycle at a current density of 500 mA g^{-1} for all subsequent cycles. As shown in **Figure 4d**, the FSO shows an excellent discharge capacity of 616.6 mAh g^{-1} after 500 cycles, with a fantastic Coulombic efficiency of 99.7%. In particular, from the 3rd to 500th cycle, the capacity retention of FSO anode is 99.4%, with an average loss of only 0.0012% per cycle, indicating the superior stability of the FSO anode. The excellent cycling

performance could be attributed to the unique core-shell structure and the relatively high conductivity of nanocrystal-FeSi phase. The appropriate thickness of SiO_x shell is the flexible buffer can effectively alleviate the volume expansion and reduce mechanical strain during cycling of Si. And the highly stable SEI film is formed on the surface of the FSO electrode due to the existence of the SiO_x shell, reducing the repeated formation of SEI film during cycles which leads to a decline in capacity. Moreover, iron oxides (Fe_2O_3 and Fe_3O_4) are converted to metallic Fe (0) nanoparticles (NPs) in a Li_2O matrix, which can stabilize the silicon SEI and effectively prevent structural damage.[50] The iron oxides not only provide anode capacity but also improve the cycle stability of the FSO electrode. **Figure S7** shows cycling performance of the FSO anodes for 1:1:1 FEC/DMC/EMC electrolyte and 1:1 EC/DEC with 5 % FEC electrolyte at a current density of 50 mA g^{-1} for the initial two cycles and at 1 A g^{-1} in the following cycles. The FSO anode for 1:1 EC/DEC with 5 % FEC shows a good cycling stability as well as the 1:1:1 FEC/DMC/EMC electrolyte. Furthermore, profiting from its high conductivity, the nanocrystal-FeSi phase enhances electron delivery. The faster of the electronic transmission reduce the polarization phenomenon which is formed by the local accumulation of electron, making more active substances are involved in the electrochemical reaction so as to improve the charge/discharge capacity of FSO. The cycling performance of FSO (obtained at 800 ^{o}C) far surpasses that of FSO-400, FSO-600 and FSO-1000. The FSO-400 and FSO-600 provide the discharge capacities of 253.8 mAh g^{-1} and 268.4 mAh g^{-1} after 500 cycles, with 24.9% and 34% capacity retention, respectively. This may be related to their inadequate SiO_x shell with not enough oxidation, which cannot prevent particle fracture from drastic volume changes during lithiation and delithiation. Furthermore, the cycle performance of FSO anodes with a high mass loading of 1.51 mg cm^{-2} and 1.98 mg cm^{-2} could retain relatively stable capacity that they could provide capacity of 608 mAh g^{-1} after 250 cycles and 561 mAh g^{-1} after 150 cycles, respectively (**Figure S8**). The Fe-Si alloy anode and FSO1000 anode show especially poor cycling performance as their discharge capacities quickly decrease to < 100 mAh g^{-1} after several cycles due to their fragile structure during the electrochemical process. In addition, the FSO also demonstrates a high rate performance. **Figure 4e** shows the rate performance of the FSO at different current densities from 50 mA g^{-1} to 10 A g^{-1}. The FSO anode provides a discharge capacity of 931.3 mAh g^{-1} at a current density of 50 mA g^{-1}, 761.8 mAh g^{-1} at 100 mA g^{-1}, 710 mAh g^{-1} at 200 mA g^{-1}, 609.6 mAh g^{-1} at 500 mA g^{-1}, 549.4 mAh g^{-1} at 1A g^{-1}, 461.9 mAh g^{-1} at 2 A g^{-1}, 333.6.8 mAh g^{-1} at 5

A g^{-1}, and 251.8 mAh g^{-1} at 8 A g^{-1}. Even at a very high current density of 10 A g^{-1}, the FSO anode still provides a capacity more than 185 mAh g^{-1}. Furthermore, a capacity more than 900 mAh g^{-1} can be retained when the current density reduce back to 50 mA g^{-1} after 50 cycles of charge and discharge at various current densities, indicating that the FSO anode has excellent rate performance and cycling stability. The detailed reaction kinetics of the FSO anode is further studied by electrochemical impedance spectroscopy (EIS) measurements. The EIS is carried out to analyze the resistance evolution between the FSO anode and Fe-Si alloy anode and the frequency range set between 100 kHz and 1 mHz. The high-frequency semicircle in EIS represents interface (SEI and charge transfer) impedance, while the low frequency line represents ion diffusion resistance. In **Figure 4f**, the Nyquist plots of the FSO anode and Fe-Si alloy anode show that the interface resistance of the FSO anode is a little higher than that of the Fe-Si alloy due to the formation of the SiO$_x$ shell. Despite the increase in interface resistance, the FSO anode still provides a very good rate performance, which may be attributed to self-conductive nanocrystal-FeSi usage as a robust mechanical skeleton to mechanically support the volume expansion change and the unique core-shell structure.

Moreover, the long-life performance of the FSO anode was investigated at a higher current density of 1 A g^{-1} for 1000 cycles after activation at a smaller current density of 50 mA g^{-1} for the initial two cycles. As shown in **Figure 4g**, after 1000 cycles, the capacity retention of the FSO anode is 86% from 3rd to 1000th cycle, with an average loss over 1000 total cycles of only 0.014% per cycle, indicating excellent cycling stability. The cycling performances of FSO anode at current densities of 50 and 200 mA g^{-1} could retain relatively stability that they could provide capacity of 967 mAh g^{-1} after 50 cycles and 727 mAh g^{-1} after 600 cycles, respectively. To the best of our knowledge, it is one of the best performances among the Si/SiO$_x$-based anodes as reported (**Table S3**). Therefore, the long cycling stability of the FSO anode confirms that the robustness of the core-shell structure particles prepared by the facile, low-cost, and scalable synthesis method can provide the possibility to commercialize Si/SiO$_x$-based Li-ion batteries. The morphological evolution of the FSO electrode after 1000 cycles is verified by SEM and TEM characterization as shown in **Figure S9**. Except for a litter crush, the FSO electrode still remained the whole structure after 1000 cycles. This demonstrates that the FSO electrode keeps its structural integrity after long-term charge and discharge processes, guaranteeing the stability of the cycling

performance of the FSO anode. Meanwhile, the XRD pattern of the FSO electrode over 1000 cycles has been provided in **Figure S10**. The phase of FeSi can still be seen in the XRD pattern after 1000 cycles, indicating that the FeSi phase does not involed in the lithium reaction and just acts as conductive agent and buffer layer [47].

The full cell with prelithiated FSO as the anode and commercial $LiCoO_2$ (LCO) as the cathode performance in the voltage range of 2.5 and 4.2 V is shown in **Figure 5** (The half-cell data of LCO is in Supporting Information, **Figure S11**). The full cell capacity was based on the weight of $LiCoO_2$ in cathode. **Figure 5a** shows the typical 1st cycle voltage profiles for the Si anode-based full cell at 0.05 C between 2.5 and 4.2 V, and the plateau appears at 3.4-3.8 V. According to the computational formula: Energy density $= \{(C_{cathode} \times C_{anode})/(C_{cathode} + C_{anode})\}V_{nominal})\}$, the cell delivers a high energy density of ~467.5 Wh kg^{-1} at 0.05 C for the first cycle with 95.9% initial Columbic efficiency, and ~355.6 Wh kg^{-1} at 0.5 C for the subsequent cycles. Details on the calculation are given in the **Supporting Information**. Moreover, the fabricated full cell system shows a good cycling stability after 50 cycles with an average columbic efficiency of 99.3% during the cycles, which could be attributed the effective prelithiation and the unique robust structure of self-conductive sub-micrometer core-shell structure FSO anode materials.

Conclusion

In summary, the sub-micrometer core-shell structure FSO anode materials are successfully prepared by a simple method using the commercial Fe-Si alloy as the Si/SiO_x source. The SiO_x shell was obtained by the oxidation of the silicon on the surface of the Fe-Si alloy particle, with the formation of nanocrystal-FeSi by in-situ reaction of the $FeSi_2$ during the phase transformation. Benefiting from the unique core-shell structure and self-conductive nanocrystal-FeSi as a robust mechanical skeleton, the FSO anode provides excellent cycling stability with 99.4% capacity retention over 500 cycles at 500 mA g^{-1}, 86% capacity retention over 1000 cycles at 1 A g^{-1}, which is one of the best performances among micrometer/sub-micrometer Si/SiO_x-based anodes reported. The excellent rate performance of the FSO anode was also demonstrated without further carbon modification, providing a discharge capacity of 333.6 mAh g^{-1} at a very high current density of 5 A g^{-1}. Moreover, the full cell with prelithiated FSO as the anode and commercial $LiCoO_2$ as the cathode

(2.5-4.2V) delivers a high energy density of ~467.5 Wh kg^{-1} at 0.05 C for the first cycle with a 95.9% initial Columbic efficiency. It should be noted that the synthesis process of sub-micrometer core-shell structure FSO anode materials is simple, environmentally friendly and cost-effective, providing a possibility to commercialize the high-performance Si/SiO$_x$-based anodes for LIBs.

Acknowledgements

References

[1] J.M. Tarascon, M. Armand, Issues and challenges facing rechargeable lithium batteries, Nature 414(6861) (2001) 359-367.

[2] M.N. Obrovac, V.L. Chevrier, Alloy negative electrodes for li-ion batteries, Chemical reviews 114(23) (2014) 11444-502.

[3] B. Dunn, H. Kamath, J.-M. Tarascon, Electrical energy storage for the grid: a battery of choices, Science 334(6058) (2011) 928-935.

[4] X. Su, Q. Wu, J. Li, X. Xiao, A. Lott, W. Lu, B.W. Sheldon, J. Wu, Silicon-Based Nanomaterials for Lithium-Ion Batteries: A Review, Advanced Energy Materials 4(1) (2014) n/a-n/a.

[5] H. Tian, F. Xin, X. Wang, W. He, W. Han, High capacity group-IV elements (Si, Ge, Sn) based anodes for lithium-ion batteries, Journal of Materiomics 1(3) (2015) 153-169.

[6] X. Huang, J. Yang, S. Mao, J. Chang, P.B. Hallac, C.R. Fell, B. Metz, J. Jiang, P.T. Hurley, J. Chen, Controllable synthesis of hollow Si anode for long-cycle-life lithium-ion batteries, Advanced materials 26(25) (2014) 4326-32.

[7] T.M. Higgins, S.-H. Park, P.J. King, C. Zhang, N. McEvoy, N.C. Berner, D. Daly, A. Shmeliov, U. Khan, G. Duesberg, V. Nicolosi, J.N. Coleman, A Commercial Conducting Polymer as Both Binder and Conductive Additive for Silicon Nanoparticle-Based Lithium-Ion Battery Negative Electrodes, ACS Nano 10(3) (2016) 3702-3713.

[8] X. Li, M. Gu, S. Hu, R. Kennard, P. Yan, X. Chen, C. Wang, M.J. Sailor, J.G. Zhang, J. Liu, Mesoporous silicon sponge as an anti-pulverization structure for high-performance lithium-ion battery anodes, Nature communications 5 (2014) 4105.

[9] J. Song, M. Zhou, R. Yi, T. Xu, M.L. Gordin, D. Tang, Z. Yu, M. Regula, D. Wang, Interpenetrated Gel Polymer Binder for High-Performance Silicon Anodes in Lithium-ion Batteries, Advanced Functional Materials 24(37) (2014) 5904-5910.

[10] S.-M. Kim, M.H. Kim, S.Y. Choi, J.G. Lee, J. Jang, J.B. Lee, J.H. Ryu, S.S. Hwang, J.-H. Park, K. Shin, Y.G. Kim, S.M. Oh, Poly(phenanthrenequinone) as a conductive binder for nano-sized silicon negative electrodes, Energy Environ. Sci.   (2015).

[11] H. Kim, M. Seo, M.H. Park, J. Cho, A critical size of silicon nano-anodes for lithium rechargeable batteries, Angewandte Chemie 49(12) (2010) 2146-9.

[12] X. Liu, Y. Gao, R. Jin, H. Luo, P. Peng, Y. Liu, Scalable synthesis of Si nanostructures by low-temperature magnesiothermic reduction of silica for application in lithium ion batteries, Nano Energy 4 (2014) 31-38.

[13] Z. Lu, N. Liu, H.-W. Lee, J. Zhao, W. Li, Y. Li, Y. Cui, Nonfilling Carbon Coating of Porous Silicon Micrometer-Sized Particles for High-Performance Lithium Battery Anodes, ACS Nano 9(3) (2015) 2540-2547.

[14] F.H. Du, B. Li, W. Fu, Y.J. Xiong, K.X. Wang, J.S. Chen, Surface binding of polypyrrole on porous silicon hollow nanospheres for Li-ion battery anodes with high structure stability, Advanced materials 26(35) (2014) 6145-50.

[15] S. Li, X. Qin, H. Zhang, J. Wu, Y.-B. He, B. Li, F. Kang, Silicon/carbon composite microspheres with hierarchical core–shell structure as anode for lithium ion batteries, Electrochemistry Communications 49 (2014) 98-102.

[16] J. Wu, X. Qin, C. Miao, Y.-B. He, G. Liang, D. Zhou, M. Liu, C. Han, B. Li, F. Kang, A honeycomb-cobweb inspired hierarchical core–shell structure design for electrospun silicon/carbon fibers as lithium-ion battery anodes, Carbon 98 (2016) 582-591.

[17] H. Tian, X. Tan, F. Xin, C. Wang, W. Han, Micro-sized nano-porous Si/C anodes for lithium ion batteries, Nano Energy 11 (2015) 490-499.

[18] X. Li, C. Yan, J. Wang, A. Graff, S.L. Schweizer, A. Sprafke, O.G. Schmidt, R.B. Wehrspohn, Stable Silicon Anodes for Lithium-Ion Batteries Using Mesoporous Metallurgical Silicon, Advanced Energy Materials 5(4) (2015) n/a-n/a.

[19] M. Li, Y. Yu, J. Li, B. Chen, X. Wu, Y. Tian, P. Chen, Nanosilica/carbon composite spheres as anodes in Li-ion batteries with excellent cycle stability, J. Mater. Chem. A 3(4) (2015) 1476-1482.

[20] X.H. Liu, L. Zhong, S. Huang, S.X. Mao, T. Zhu, J.Y. Huang, Size-Dependent Fracture of Silicon Nanoparticles During Lithiation, ACS Nano 6(2) (2012) 1522-1531.

[21] Y. Li, K. Yan, H.-W. Lee, Z. Lu, N. Liu, Y. Cui, Growth of conformal graphene cages on micrometre-sized silicon particles as stable battery anodes, Nature Energy 1(2) (2016) 15029.

[22] B. Zhu, Y. Jin, Y. Tan, L. Zong, Y. Hu, L. Chen, Y. Chen, Q. Zhang, J. Zhu, Scalable Production of Si Nanoparticles Directly from Low Grade Sources for Lithium-Ion Battery Anode, Nano letters 15(9) (2015) 5750-4.

[23] J. Wang, X. Meng, X. Fan, W. Zhang, H. Zhang, C. Wang, Scalable Synthesis of Defect Abundant Si Nanorods for High-Performance Li-Ion Battery Anodes, ACS Nano 9(6) (2015) 6576-6586.

[24] M. Ge, Y. Lu, P. Ercius, J. Rong, X. Fang, M. Mecklenburg, C. Zhou, Large-Scale Fabrication, 3D Tomography, and Lithium-Ion Battery Application of Porous Silicon, Nano letters 14(1) (2014) 261-268.

[25] W. He, H. Tian, F. Xin, W. Han, Scalable fabrication of micro-sized bulk porous Si from Fe-Si alloy as a high performance anode for lithium-ion batteries, Journal of Materials Chemistry A 3(35) (2015) 17956-17962.

[26] M.-S. Park, E. Park, J. Lee, G. Jeong, K.J. Kim, J.H. Kim, Y.-J. Kim, H. Kim, Hydrogen Silsequioxane-Derived Si/SiOx Nanospheres for High-Capacity Lithium Storage Materials, ACS applied materials & interfaces 6(12) (2014) 9608-9613.

[27] X. Bai, Y. Yu, H.H. Kung, B. Wang, J. Jiang, Si@SiOx/graphene hydrogel composite anode for lithium-ion battery, Journal of Power Sources 306 (2016) 42-48.

[28] L. Zhang, J. Deng, L. Liu, W. Si, S. Oswald, L. Xi, M. Kundu, G. Ma, T. Gemming, S. Baunack, F. Ding, C. Yan, O.G. Schmidt, Hierarchically Designed SiOx/SiOy Bilayer Nanomembranes as Stable Anodes for Lithium Ion Batteries, Advanced materials 26(26) (2014) 4527-4532.

[29] J.-I. Lee, K.T. Lee, J. Cho, J. Kim, N.-S. Choi, S. Park, Chemical-Assisted Thermal Disproportionation of Porous Silicon Monoxide into Silicon-Based Multicomponent Systems, Angewandte Chemie International Edition 51(11) (2012) 2767-2771.

[30] J. Wang, M. Zhou, G. Tan, S. Chen, F. Wu, J. Lu, K. Amine, Encapsulating Micro-Nano Si/SiOx into Conjugated Nitrogen-Doped Carbon as Binder-Free Monolithic Anodes for Advanced Lithium Ion Batteries, Nanoscale   (2015).

[31] D. Wang, M. Gao, H. Pan, J. Wang, Y. Liu, High performance amorphous-Si@SiOx/C composite anode materials for Li-ion batteries derived from ball-milling and in situ carbonization, Journal of Power Sources 256 (2014) 190-199.

[32] Q. Huang, E.D. Walter, L. Cosimbescu, D. Choi, J.P. Lemmon, In situ electrochemical-electron spin resonance investigations of multi-electron redox reaction for organic radical cathodes, Journal of Power Sources 306 (2016) 812-816.

[33] Y. Chen, L. Liu, J. Xiong, T. Yang, Y. Qin, C. Yan, Porous Si Nanowires from Cheap Metallurgical Silicon Stabilized by a Surface Oxide Layer for Lithium Ion Batteries, Advanced Functional Materials 25(43) (2015) 6701-6709.

[34] L. Sun, T. Su, L. Xu, M. Liu, H.-B. Du, Two-dimensional ultra-thin SiOx (0 < x < 2) nanosheets with long-term cycling stability as lithium ion battery anodes, Chemical communications 52(23) (2016) 4341-4344.

[35] J. Niu, S. Zhang, Y. Niu, H. Song, X. Chen, J. Zhou, B. Cao, Direct amination of Si nanoparticles for the preparation of Si@ultrathin SiOx@graphene nanosheets as high performance lithium-ion battery anodes, Journal of Materials Chemistry A 3(39) (2015) 19892-19900.

[36] E. Park, H. Yoo, J. Lee, M.-S. Park, Y.-J. Kim, H. Kim, Dual-Size Silicon Nanocrystal-Embedded SiOx Nanocomposite as a High-Capacity Lithium Storage Material, ACS Nano 9(7) (2015) 7690-7696.

[37] K.W. Lim, J.I. Lee, J. Yang, Y.K. Kim, H.Y. Jeong, S. Park, H.S. Shin, Catalyst-free synthesis of Si-SiOx core-shell nanowire anodes for high-rate and high-capacity lithium-ion batteries, ACS applied materials & interfaces 6(9) (2014) 6340-5.

[38] S. Yoo, J.-I. Lee, M. Shin, S. Park, Large-Scale Synthesis of Interconnected Si/SiOx Nanowire Anodes for Rechargeable Lithium-Ion Batteries, ChemSusChem 6(7) (2013) 1153-1157.

[39] E. Schurmann, U. Hensgen, Studies of the Melting Equilibria in the System Iron--Silicon, Arch. Eisenhuttenwes.

51(1) (1980) 1-4.

[40] M. Li, J. Gu, X. Feng, H. He, C. Zeng, Amorphous-silicon@silicon oxide/chromium/carbon as an anode for lithium-ion batteries with excellent cyclic stability, Electrochimica Acta 164 (2015) 163-170.

[41] H.J.T. Ellingham, Transactions and Communications, Journal of the Society of Chemical Industry 63(5) (1944) 125-160.

[42] J. Liang, X. Li, Z. Hou, W. Zhang, Y. Zhu, Y. Qian, A Deep Reduction and Partial Oxidation Strategy for Fabrication of Mesoporous Si Anode for Lithium Ion Batteries, ACS Nano 10(2) (2016) 2295-304.

[43] N. Lin, Y. Han, L. Wang, J. Zhou, J. Zhou, Y. Zhu, Y. Qian, Preparation of nanocrystalline silicon from SiCl4 at 200 degrees C in molten salt for high-performance anodes for lithium ion batteries, Angewandte Chemie 54(12) (2015) 3822-5.

[44] Z.-L. Xu, B. Zhang, J.-K. Kim, Electrospun carbon nanofiber anodes containing monodispersed Si nanoparticles and graphene oxide with exceptional high rate capacities, Nano Energy 6 (2014) 27-35.

[45] Y. Xu, Y. Zhu, F. Han, C. Luo, C. Wang, 3D Si/C Fiber Paper Electrodes Fabricated Using a Combined Electrospray/Electrospinning Technique for Li-Ion Batteries, Advanced Energy Materials 5(1) (2015) n/a-n/a.

[46] Y. Jin, S. Zhang, B. Zhu, Y. Tan, X. Hu, L. Zong, J. Zhu, Simultaneous Purification and Perforation of Low-Grade Si Sources for Lithium-Ion Battery Anode, Nano letters 15(11) (2015) 7742-7.

[47] M.X. Gao, D.S. Wang, X.Q. Zhang, H.G. Pan, Y.F. Liu, C. Liang, C.X. Shang, Z.X. Guo, A hybrid Si@FeSiy/SiOx anode structure for high performance lithium-ion batteries via ammonia-assisted one-pot synthesis, Journal of Materials Chemistry A 3(20) (2015) 10767-10776.

[48] S. Jing, H. Jiang, Y. Hu, C. Li, Graphene supported mesoporous single crystal silicon on Cu foam as a stable lithium-ion battery anode, J. Mater. Chem. A 2(39) (2014) 16360-16364.

[49] C. Xiao, N. Du, X. Shi, H. Zhang, D. Yang, Large-scale synthesis of Si@C three-dimensional porous structures as high-performance anode materials for lithium-ion batteries, J. Mater. Chem. A 2(48) (2014) 20494-20499.

[50] G. Grinbom, D. Duveau, G. Gershinsky, L. Monconduit, D. Zitoun, Silicon/Hollow γ-Fe2O3 Nanoparticles as Efficient Anodes for Li-Ion Batteries, Chemistry of Materials 27(7) (2015) 2703-2710.
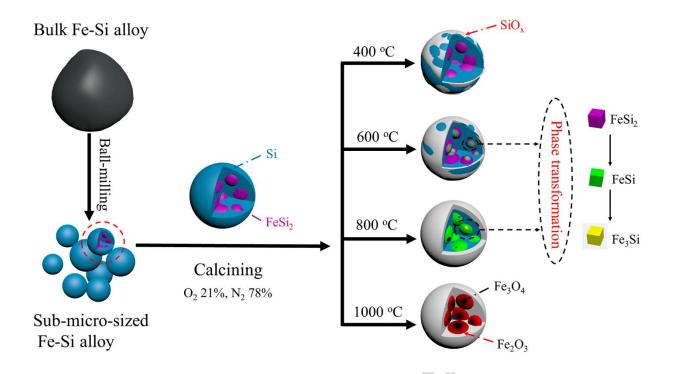
Figure1. The schematic drawing of the ball-milling and the calcing process for the preparation of FSO anode materials.
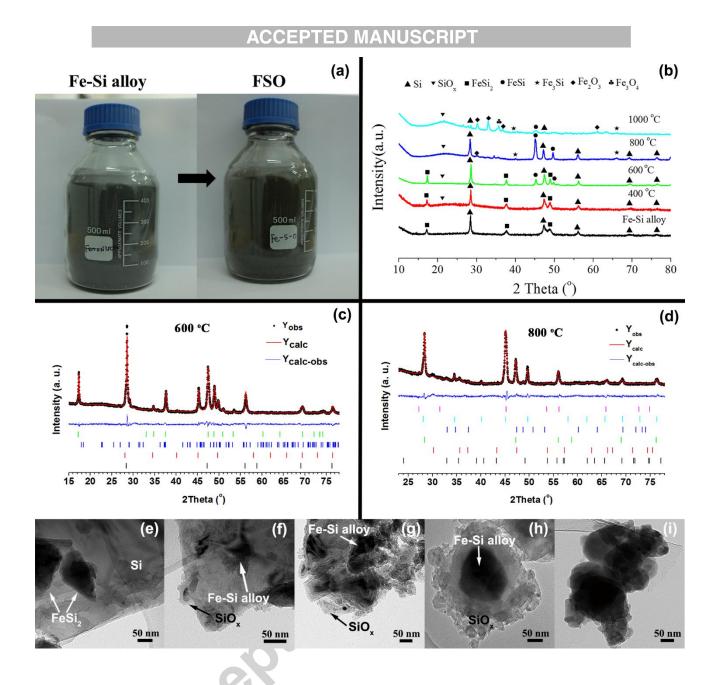
.

Figure 2. (a) Photograph of the high production of FSO anode materials. (b)The XRD results of the Fe-Si alloy before and after calcination at various temperatures. (c, d) The Rietveld refinement of the XRD peaks from samples heated at 600 ^{o}C and 800 ^{o}C, respectively. The ticks used in refinement are tetragonal $FeSi_2$ (green), orthorhombic $FeSi_2$ (blue), FeSi (red), and Si (black) for (c). Ticks in (d) are Fe_3Si (magenta), FeSi (cyan), $FeSi_2$ (blue), Si (green), Fe_3O_4 (red), and Fe_2O_3 (black). (e)-(i) are the TEM images of the Fe-Si alloy before calcination (e), after calcination at 400 ^{o}C (f), 600 ^{o}C (g), 800 ^{o}C (h), and 1000 ^{o}C (i).
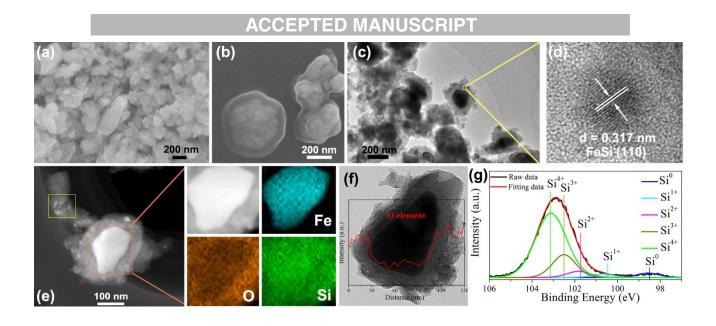
Figure 3. SEM images of FSO particles, obtained at 800 °C with low magnification (a) and high magnification (b). TEM image (c) and corresponding high-resolution TEM image (d) of the FSO obtained at 800 °C. (e) EDS elemental mapping results of FSO, (f) STEM and O intensity line scan of the FSO, (g) X-ray photoelectron spectroscopy analysis of the FSO anode materials.
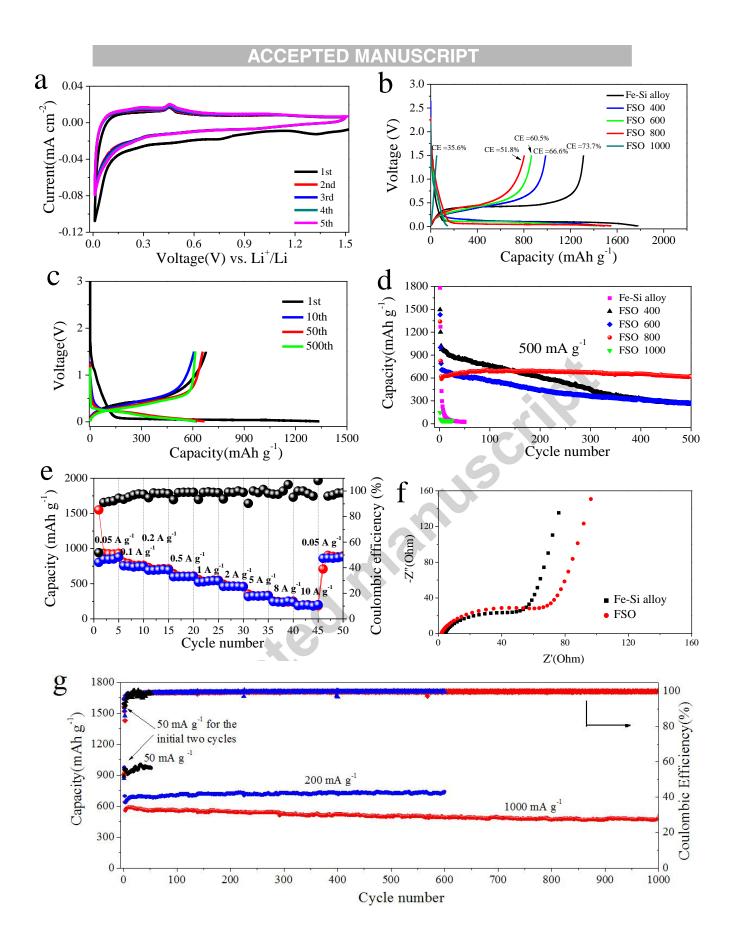
Figure 4. Electrochemical performance of FSO anodes. (a) Cyclic voltammetry of the initial 5 cycles of the FSO anode at a scan rate of 0.1 mV s^{-1} from 1.5 V to 0.01 V. (b) Charge/discharge profiles of the FSO and Fe-Si alloy anodes at the first cycle. (c) Charge/discharge profiles of the FSO anode at the first, 10th, 50th and 500th cycle. (d) Cycling performance of the Fe-Si alloy and FSO anode which was treated at different temperatures at a current density of 50 mA g^{-1} for the initial two cycles and at 500 mA g^{-1} for the following cycles. (e) Rate capacity of the FSO anode between 0.01 V and 1.5 V at various rates (50 mA g^{-1}-100000 mA g^{-1}) (f) Nyquist plots of the electrodes of the FSO anode and Fe-Si alloy to 1.5 V. (Z' and Z" denote real and imaginary parts, respectively). (g) Cycling property of the FSO electrode.
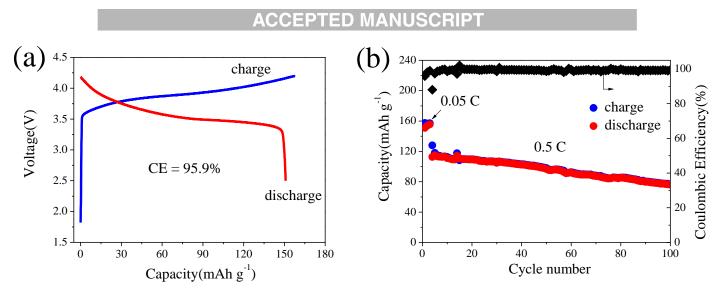
Figure 5. Electrochemical characterization of the full cell with prelithiated FSO as the anode and commercial LiCoO$_2$ as the cathode. (a) galvanostatic charge and discharge profile of the first cycle between 2.5 and 4.2 V at the current density rate of 0.05 C; (b) Cycling performance between 2.5 and 4.2 V at 0.05 C for the initial three cycles and at 0.5 C in the following cycles.

Table-of-Contents Graphic